



# Early Detection and Analysis of an Unpredicted Convective Storm over the Negev Desert

Shilo Shiff <sup>1,\*</sup> , Amir Givati <sup>2</sup>, Steve Brenner <sup>1</sup> and Itamar M. Lensky <sup>1</sup>

<sup>1</sup> Department of Geography and Environment, Bar-Ilan University, Ramat Gan 5290002, Israel; itamar.lensky@biu.ac.il (I.M.L.)

<sup>2</sup> Environmental Studies Department, Porter School of the Environmental and Earth Sciences, Tel Aviv University, Tel Aviv 6997801, Israel

\* Correspondence: shilo.shiff@biu.ac.il

**Abstract:** On 15 September 2015, a convective storm yielded heavy rainfalls that caused the strongest flash flood in the last 50 years in the South Negev Desert (Israel). None of the operational forecast models predicted the event, and thus, no warning was provided. We analyzed this event using satellite, radar, and numerical weather prediction model data. We generated cloud-free climatological values on a pixel basis using Temporal Fourier Analysis on a time series of MSG geostationary satellite data. The discrepancy between the measured and climatological values was used to detect “cloud-contaminated” pixels. This simple, robust, fast, and accurate method is valuable for the early detection of convection. The first clouds were detected 30 min before they were detected by the official MSG cloud mask, 4.5 h before the radar, and 10 h before the flood reached the main road. We used the “severe storms” RGB composite and the satellite-retrieved vertical profiles of cloud top temperature–particle’s effective radius relations as indicators for the development of a severe convective storm. We also reran the model with different convective schemes, with much-improved results. Both the satellite and model-based analysis provided early warning for a very high probability of flooding a few hours before the actual flooding occurred.

**Keywords:** convective storm; flash floods; cloud detection; nowcasting



**Citation:** Shiff, S.; Givati, A.; Brenner, S.; Lensky, I.M. Early Detection and Analysis of an Unpredicted Convective Storm over the Negev Desert. *Remote Sens.* **2023**, *15*, 5241. <https://doi.org/10.3390/rs15215241>

Academic Editors: Stefano Federico, Rosa Claudia Torcasio, Martina Lagasio and Vincenzo Mazzarella

Received: 14 September 2023

Revised: 31 October 2023

Accepted: 1 November 2023

Published: 4 November 2023



**Copyright:** © 2023 by the authors. Licensee MDPI, Basel, Switzerland. This article is an open access article distributed under the terms and conditions of the Creative Commons Attribution (CC BY) license (<https://creativecommons.org/licenses/by/4.0/>).

## 1. Introduction

Extreme rain events can lead to flash floods that can cause heavy damage to crops, soil erosion, infrastructure, environmental ecosystems, and even human life. In recent decades, the frequency of severe weather events has been increasing and is expected to increase even more (e.g., [1]), driven by rising global temperatures and other climatic changes. Early warnings can minimize the damage caused by extreme weather events. However, forecasting flash floods is considered a very challenging mission, especially in arid areas, due to their rapid development [2,3] and small spatial scale. Proper calibration and data assimilation can improve the convection-permitting rainfall forecast models and hydrological models, which in turn will improve the predictability of flash-flood forecasts, but in less occupied arid regions, the possibility to improve these models is limited as monitoring instruments such as rain radars and rain gauges are rare [4], and gaps in information exist.

Physical parameterization schemes in numerical weather prediction models (NWP) are used to represent sub-grid processes that the model cannot explicitly simulate, such as convective processes. There are many different schemes available, each representing the sub-grid processes in different ways, e.g., some convective parameterizations account for the effects of shallow convection on the environment, others account for the effects of deep convection, and some account for both. These schemes are crucial in determining how accurately the model simulates localized features that are important for daily activities, such as high and low temperatures, rainfall, cloudiness, and winds. Choosing the “correct”

convective scheme can have a major impact on forecasting flash floods in arid regions, as in the case presented in this study.

Flash floods occur when a riverbed cannot contain the flow. They will occur when favorable meteorological conditions (the amount and intensity of the precipitation in a single event or the accumulated precipitation of sequential events) and hydrological conditions (hydrological, lithological, geomorphological, and topographic) conditions exist simultaneously.

On 15 September 2015, an intense convective storm developed over the Sinai Peninsula. The storm yielded heavy rainfalls that caused the strongest flash flood in the South Negev Desert in the last 50 years. This event was unique not only due to its intensity but also due to its early occurrence before the rainy season, which usually begins in October. The storm had occurred with no warning, and none of the operational forecast models predicted the event. This storm was associated with a “Red Sea trough” (RST, see Figure 1), which is a low-pressure system extending from the south, over the Red Sea towards the eastern Mediterranean and the Levant [5–8] occurring most frequently during fall and spring [9,10]. However, most of the RSTs are not accompanied by rain [11–13]. Occasionally, the RST is accompanied by a pronounced upper-level trough that develops over Egypt and, at times, initiates convective storms over the Levant.

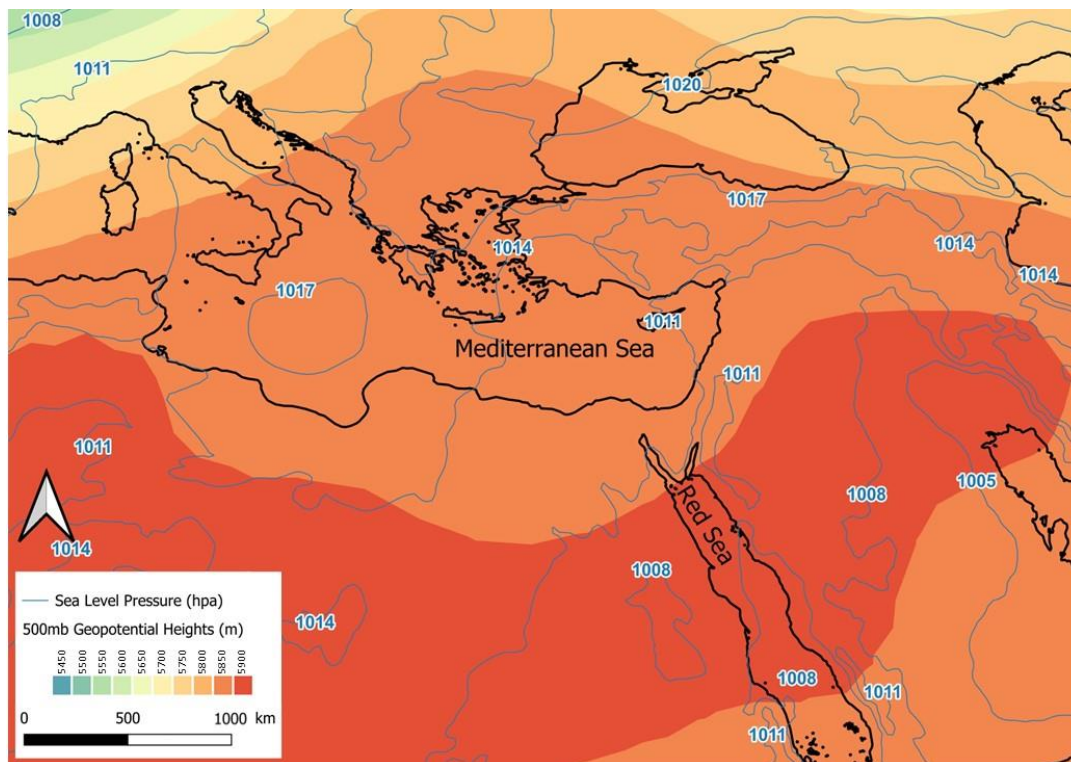


**Figure 1.** Geopotential height at 500 hPa (color scale) and sea level pressure (blue contours) for 15 September 2015 at 12:00 UTC.

The event analyzed in this paper occurred in an arid region and the convection initiation was difficult to predict due to the absence of appropriate radar data and a forecast model with a tuned convective parameterization scheme. In this paper, we demonstrate the potential sensitivity of the NWP model simulations to the choice of the convective parameterization scheme. We also describe a new method of cloud detection by satellite data (which has clear advantages over radar data) that is preferable to other methods due to its early detection capability with fewer false alarms. For this event, we demonstrate the use of satellite data for the early detection of cloud development. We then follow the storm development using a multispectral analysis of the cloud’s microphysical properties.

## 2. Materials and Methods

### 2.1. The Study Area

On 15 September 2015, a convective storm developed over the Sinai Peninsula and moved east-northeastward into the southern Negev desert over the Paran watershed (Figure 2). The storm yielded heavy rainfalls that caused flash floods. A rare discharge peak of  $913 \text{ m}^3/\text{s}^{-1}$  was recorded at the Paran River's "Bottleneck" 57165 station. This was the second highest peak recorded, second only to the event of 11 June 1970, with  $1160 \text{ m}^3/\text{s}^{-1}$ . The probability of such a high discharge amount is 2% or once in 50 years [14]. This event was unique not only due to its intensity but also due to its early occurrence before the rainy season, which usually begins in October [8]. The Israeli Hydrological Service has no other record of such an intense event that occurred so early in the transition season.

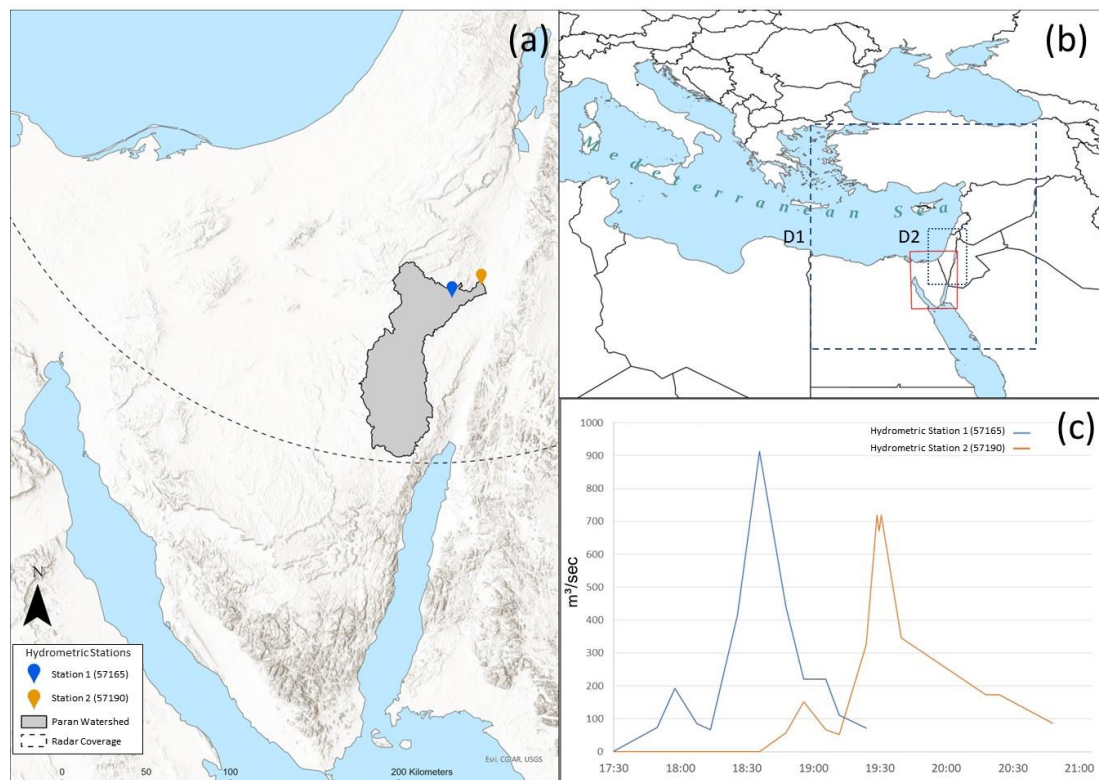


**Figure 2.** (a) Location of the Paran watershed and surrounding area, the IMS radar extent (indicated by the dashed curve), and the location of the two hydrometric stations. (b) Location of the study area (red rectangle) relative to the Eastern Mediterranean Sea. Model nested domains: D1 (9 km resolution—dashed line rectangle), D2 (3 km resolution—dotted line rectangle). (c) Flood hydrographs of Paran watershed for the 15 September 2015 event at stations 57165 and 57190.

### 2.2. Observations (Satellite, Radar, Hydrometric Measurements, and Radiosondes)

#### 2.2.1. Satellite Data

We used data from the Spinning Enhanced Visible and Infrared Imager (SEVIRI) onboard the European geostationary Meteosat Second Generation (MSG) satellite operated by EUMETSAT. SEVIRI has 11 spectral channels with 3 km spatial resolution at the nadir and one High-Resolution Visible (HRV) channel (1 km at the nadir), all operationally available at 15 min temporal resolution [15]. The archived data are freely available at the Eumetsat Earth Observation portal.

Moderate Resolution Imaging Spectroradiometer (MODIS) aboard the Aqua polar-orbiting sun-synchronous satellite has 36 spectral channels. The equator crossing time for Aqua is 13:30 local solar time. We used the Google Earth Engine platform to download the MODIS Aqua 250 m spatial resolution surface reflectance product (MYD09GQ), red

(620–670 nm), and near-infrared (841–876 nm) bands [16]. We used the MODIS image to assess the MSG cloud mask. Time series of 1 pixel of MODIS (MYD09GA.061) ch01 surface reflectance and ch31 brightness temperature were downloaded from <https://appears.earthdatacloud.nasa.gov/task/point> (accessed on 31 October 2023) to demonstrate the cloud detection concept proposed in this paper.

### 2.2.2. Radar Data

The radar data used here are from a C-Band Doppler radar located at the Israeli Meteorological Service (IMS) headquarters in Bet-Dagan (32.01°N, 34.85°E). The Paran watershed is about 250 km away from the IMS radar. At this distance, precipitation below 5 km altitude is below the lowest radar beam and, therefore, cannot be detected by the radar [17].

### 2.2.3. Hydrometric Measurements

Two active hydrometric stations of the Israel Hydrological Service (IHS) are located in the northern part of the Paran basin (3600 km<sup>2</sup>). Hydrometric station 57190 (Station 1) is located near the stream's outlet, while station 57165 (Station 2) is a few kilometers up the creek. (Figure 2a). Flood hydrographs for both stations are presented in Figure 2c. A rare discharge peak of 913 m<sup>3</sup>/s<sup>-1</sup> was recorded at station 2 at 18:40 UTC. Although this is a typical hydrograph of flood events caused by RST systems, represented by a pointed, single-peaked hydrograph with a relatively high peak discharge and short duration [18], it was unusual in its intensity (once in 50 years).

### 2.2.4. Radiosondes

Convective available potential energy (CAPE) is a measure of energy available for convection [19] traditionally derived using radiosondes. Radiosondes provide temperature, humidity, air pressure, and wind velocity profiles. The IMS radiosonde data in Israel are available twice daily, launched from Bet-Dagan, about 250 km away from the Paran watershed. The maximum CAPE measured at Bet Dagan was 2476 J kg<sup>-1</sup> 6 h before the storm and 3228 J kg<sup>-1</sup> 6 h after the storm left the watershed. CAPE values of 1000 J kg<sup>-1</sup> are generally sufficient to initiate convective storms, while values in the range of 2500–4000 J kg<sup>-1</sup> are indicative of strong instability.

## 2.3. Numerical Model Description

For this study, we used the Weather Research and Forecasting (WRF) model version 4.3.1, which is run by the Israel Hydrological Service. WRF is a state-of-the-art, highly configurable, mesoscale numerical weather prediction model designed for both operational forecasting and research. It is a fully compressible, Eulerian, non-hydrostatic model. The model was set up with two nested domains with resolutions of 9 and 3 km (Figure 2b). The boundary conditions for the outer 9 km domain were taken from the 0.25° resolution NOAA/NCEP Global Forecasting System (GFS) reanalysis, which is available at 6 h intervals. The subgrid-scale parameterization schemes in the model were chosen following Givati et al. [20], who tested and configured the model to provide precipitation forecasts as input for a hydrological model of the upper Jordan River catchment area and streamflow. These schemes included the Morrison double-moment cloud microphysics scheme, the NOAH land surface model, and the level 1.5 moment closure TKE-based planetary boundary layer scheme.

Two 72 h simulations were run, both initialized at 00 UTC on 15 September 2015, which was roughly 12 h before the convective event began. The two simulations differed only in the choice of the convective parameterization scheme in the 9 km domain. The convective scheme is not activated in the higher-resolution domain. The default simulation used the Grell 3D ensemble scheme [21] in which a large ensemble of closure assumptions and parameters are used to determine the relevant values that are fed back into the three-dimensional model. The closures and parameters in the ensemble are based on

cumulus parameterization schemes, which are currently used in various forecast models. As described below, this simulation underestimated the intensity of the rainfall and the location of the convective cells, and therefore, a second simulation was run with an alternative convective parameterization scheme, which is the most likely source of the under-estimated precipitation. In this case, the Kain–Fritsch scheme [22], which is a mass flux parameterization, was used. It is based on a Lagrangian parcel method to estimate whether instability exists and to determine if any existing instability will become available for cloud growth, as well as the properties of any clouds that may form. It should be noted that any further investigation of the parameterization schemes is beyond the scope of this study. The microphysics and other parameterization schemes were selected based on the WRF configuration for this region recommended in [20] after extensive testing.

#### 2.4. Cloud Detection in Early Stages

Identifying cloudy pixels in satellite images is an important pre-processing step in convective storm prediction. In general, clouds are colder and have higher reflectance than land and sea surfaces. Nevertheless, satellite data interpretation is complicated since the radiance received by the sensor varies with location, time, and wavelength [23]. Radiative properties of the surface may depend on soil type, vegetation, humidity, viewing, and solar angles, all of which affect surface reflectance, emissivity, and Brightness Temperature (BT). The lack of knowledge of current surface properties forces threshold-based cloud detection algorithms to apply dozens of thresholds on the different channel data. Among these algorithms are MOD35\_L2 and MYD35\_L2 for MODIS Cloud Mask [24] and MSGCLM [25] for MSG. However, accurate knowledge of the surface properties in each pixel would solve these problems and simplify the cloud detection process.

Following Scharlemann et al. [26] and Lensky and Dayan [27], we used Temporal Fourier Analysis (TFA) to describe the seasonal cycles of surface brightness temperature (BT) and reflectance in terms of multi-annual harmonics, each described by its phase and amplitude. We then retained the three leading harmonics (annual, bi-annual, and tri-annual) to create a smoothed signal that is considered to be the climatological expected BT or reflectance.

To build the TFAs, we used nine years (2004–2012) of hourly data in a domain of  $621 \times 401$  MSG pixels (resolution of 3 km at nadir) over the Eastern Mediterranean Sea. These data included channel 1 (0.6  $\mu\text{m}$ ) visible and channel 9 (10.8  $\mu\text{m}$ ) thermal infrared radiation. The same two channels exist in MODIS as channels 01 and 31, respectively. Figure 3 demonstrates the behavior of the signal of MODIS ch01 (Figure 3a) and MODIS ch31 (Figure 3b) on a single pixel in the Paran watershed for a whole year. The TFA line on the graph represents the climatological values. For a clear sky, the reflectance and BT values are very close to the TFA, whereas when a cloud covers the pixel, a significant rise in the surface reflectance and a notable drop in the BT are seen.

The TFA is calculated in two iterations. In the first iteration, any pixels suspected of being contaminated with clouds are removed, so the final TFA represents clear-sky surface climatology. We used the actual reflectance and BT deviation from the climatological values (TFA) for each pixel to detect clouds. The proposed TFA-based Cloud Mask (TFACLM) algorithm provides a way to circumvent the difficulties mentioned above by applying the climatological values of each pixel (location) and time. Beyond a small, fixed threshold, even a slight deviation from these climatological values indicates that the pixel is contaminated by clouds or aerosols.

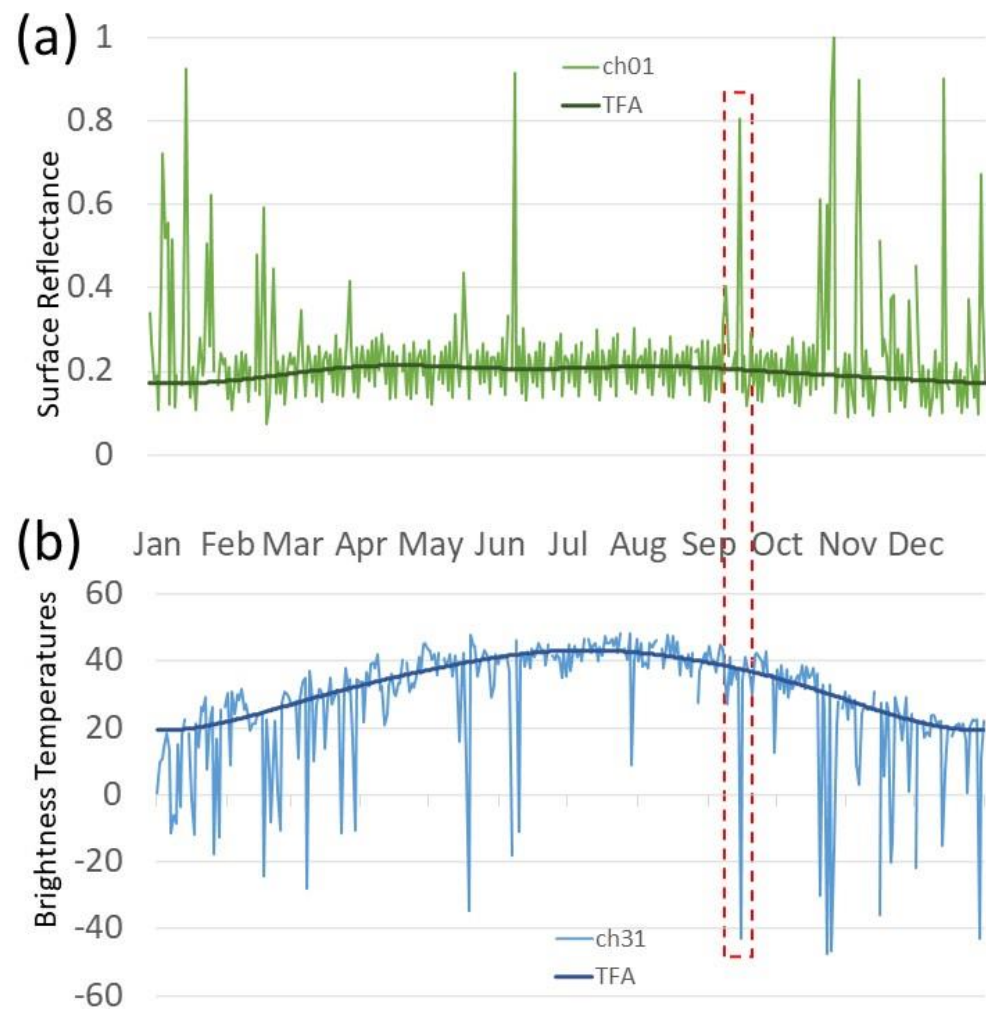


**Figure 3.** Time series of 2015 MODIS data for one pixel in Paran watershed: (a) Channel 01 surface reflectance (green), and (b) channel 31 brightness temperatures (blue). The distinct anomalies from the TFA of both channels on the day of the event (15 September 2015) are highlighted with a red dashed box.

### 2.5. Cloud Microphysics and Severe Storms

A major driving force of severe weather phenomena is strong updrafts, which are necessary for vertically displacing the rapidly converging air below the cloud. These updrafts are necessary to sustain the growth of large hailstones. Severe storms can be detected in satellite data using qualitative and quantitative methods. Among the qualitative methods are RGB combinations such as the Day Microphysical RGB and Convective Storms RGB [28]. The Convective Storms RGB is sensitive to clouds with small particles near cloud tops that are attributed to very strong updrafts, which allows less time for the cloud drops to grow by coalescence. Strong updrafts also delay the development of a mixed-phase cloud and its eventual glaciation to colder temperatures [29]. These cloud tops are noticeable by their intense yellow colors in the Convective Storms RGB. Optically thick clouds with small ice particles near their tops appear orange in the Day Microphysical RGB. As a quantitative method, Rosenfeld and Lensky [30] suggested using the evolution of cloud top effective radius ( $r_e$ , which is the ratio of the third to the second moment of a droplet size distribution [31] with height (or cloud top temperature,  $T$ ), i.e.,  $T$ - $r_e$  profile, to track the cloud particles'  $r_e$ -evolution in convective clouds. This was based on the assumption that the evolution of cloud top  $r_e$  with height observed by the satellite at a given time (snapshot) for a cloud ensemble over an area is similar to the  $T$ - $r_e$  time evolution of a given cloud at

one location [32]. These processes in severe storms are evident in the T- $r_e$  profile plots as the development of  $r_e$  is shifted to greater heights and lower temperatures.

### 3. Results

In this study, we analyze the 15 September 2015 event. This event was missed by the Israel Water Authority's forecast model (WRF Hydro). In such situations, radar and satellite observations can compensate for the missing information expected from the models. Figure 4 shows the first rain clouds detected over the Paran watershed in the northern Sinai Peninsula by the IMS radar at 12:50 UTC, hinting at potential flood risk about 4 h before the first signals from the two hydrometric stations (and 5 h before the flood reached the road).

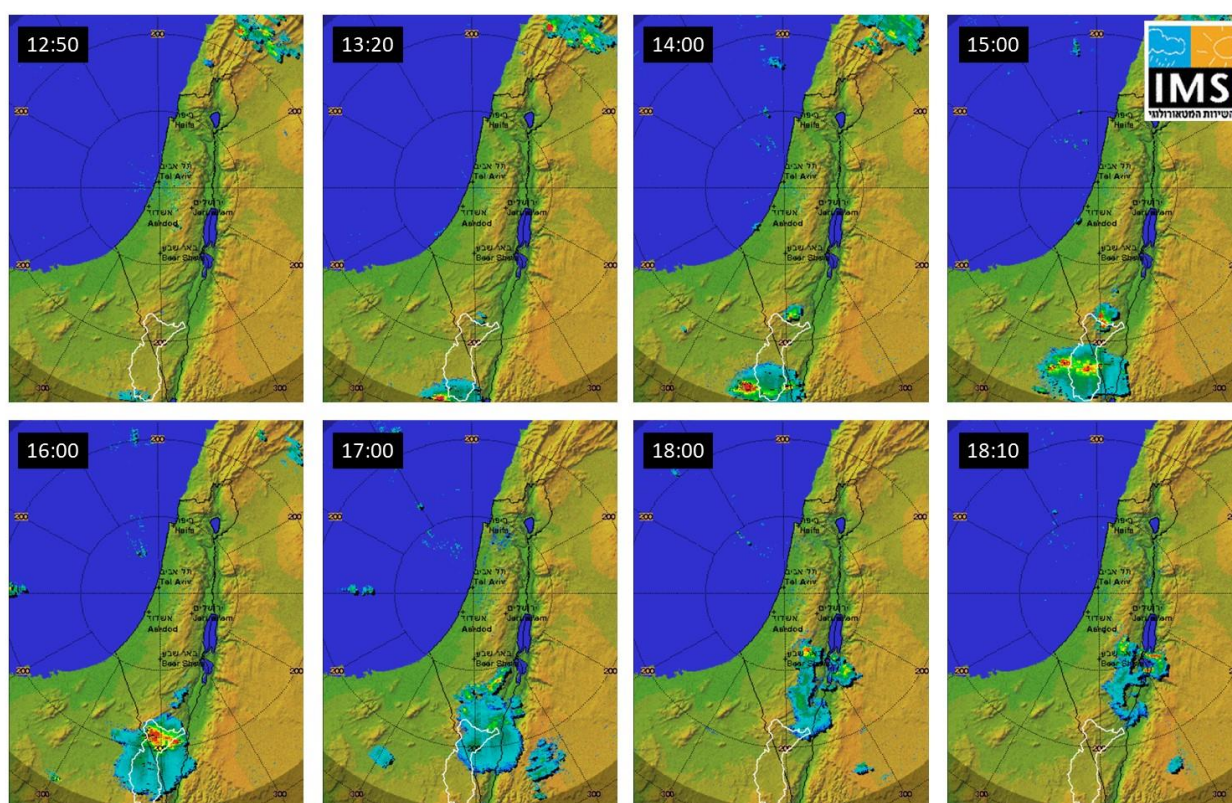


**Figure 4.** The IMS radar on 15 September 2015. The Paran watershed is outlined in white. At 12:50 UTC, a rain cloud was detected for the first time over the southwestern Paran watershed. The last cloud was detected over the northeastern corner of the watershed at 18:00.

Figure 5 shows information from MSG regarding the severity of the storm. The yellow colors of cloud tops in the Convective Storms RGB (lower row) indicate that the rain clouds detected by the IMS radar are severe convective storms. The orange colors in the Day Microphysical RGB scheme (middle row) suggest that the clouds are optically thick, with small ice particles near their tops. The T- $r_e$  plots (upper row) also support the impression that this is a severe storm event, with very small effective radii ( $r_e < 5 \mu\text{m}$ ) at the cloud base and small ice particles ( $r_e < 40 \mu\text{m}$ ) at the cloud top [29,30]. Other indicators that the vigorous cloud growth is leading to convective initiation can be characterized by subfreezing cloud top and significant cooling rates [33,34]. Three consecutive brightness temperature images are required. The first step is to identify the occurrence of a subfreezing cloud top. The second step is to ensure that the cumulus cloud evolves from a warm cloud. The third step is to ensure persistent growth of the cumulus cloud. In our case, the first yellow pixels in the Convective Storms RGB were spotted clearly as early as 11:15 UTC, while a cooling rate of  $\geq 4 \text{ }^\circ\text{C} (15 \text{ min})^{-1}$  [35,36], and the occurrence of a subfreezing cloud top, was already detected at 9:30.

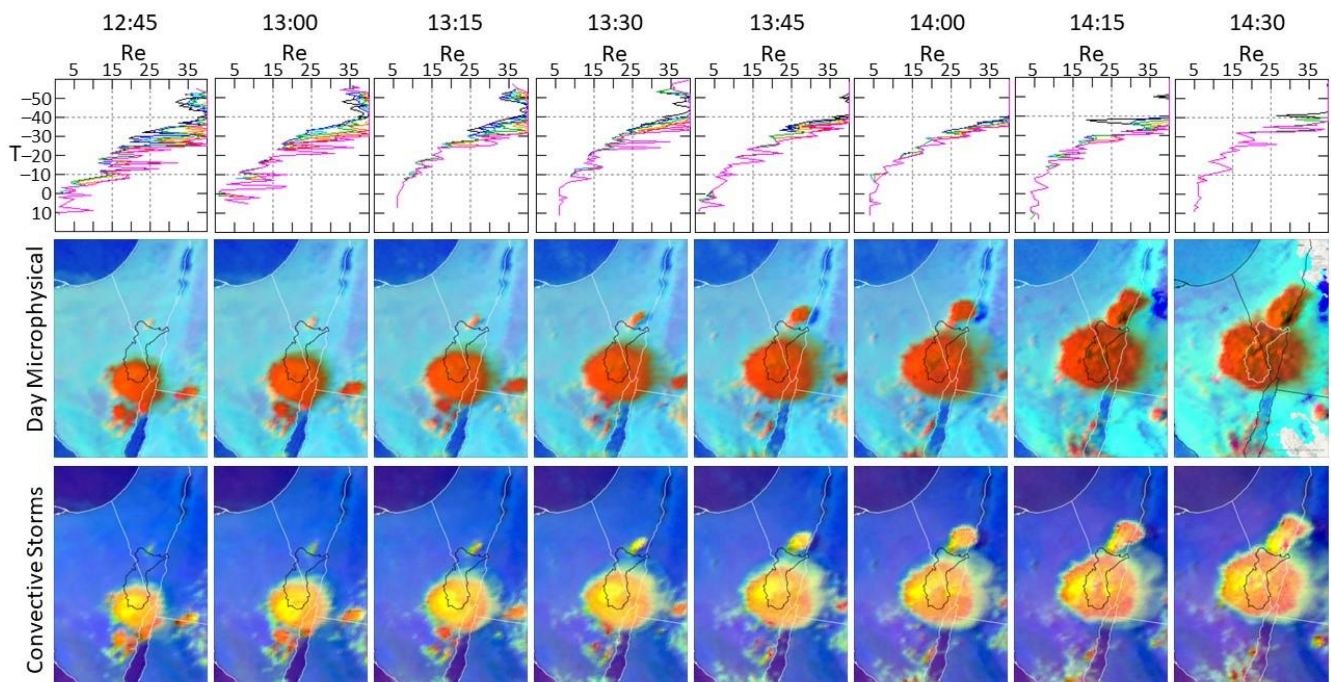


**Figure 5.** Time series of Convective Storms RGB images (lower row), MSG Day Microphysical RGB (middle row), and  $T-r_e$  plots (upper row) from 12:45 to 14:30 UTC. The bright yellow in the Convective Storms RGB indicates a severe convective storm. Optically thick clouds with small ice particles near their tops appear orange in the Day Microphysical RGB. The  $T-r_e$  curves are typical for severe storms with very small cloud droplets at the cloud base ( $r_e < 5 \mu\text{m}$ ), and small ice particles at the cloud top ( $r_e < 40 \mu\text{m}$ ).

As noted previously, this extreme event was associated with an unusual RST. It was not predicted by the Israel Water Authority's WRF Hydro model, which is used for flash flood forecasting. Most of the rain in Israel is attributed to synoptic systems with westerly flow [8,37] approaching from the Eastern Mediterranean. The model may have missed this event since it is configured to provide better forecasts for the more common rain-producing synoptic systems. To better understand the reasons for this miss by the model, we reran the WRF configured using two different convective parameterization schemes.

Figure 6 shows the results from the two simulations, one with the Grell 3D ensemble scheme (Figure 6a, left column) and the other with the Kain–Fritsch scheme (Figure 6b, middle column). Both schemes simulated the rain event approaching the Paran watershed from the Sinai Peninsula before it was observed by the IMS radar at 12:00 UTC (Figure 6c) and reasonably predicted the timing and location of the first radar echo at 13:00 UTC. At 14:00 UTC and 15:00 UTC, both simulations diverge in space and intensity from the radar observations. At 14:00 UTC, both simulations show the leading cloud cluster too far to the east. In the Grell 3D simulation, the cloud has nearly disappeared, while the Kain–Fritsch scheme shows the cloud covering a larger area with more intense precipitation. At 15:00, the better performance of the Kain–Fritsch scheme is even more pronounced in terms of cloud location and precipitation intensity. The Grell 3D scheme advances the cloud too far to the east, extending into the Kingdom of Jordan, while the Kain–Fritsch scheme maintains the cloud's position over the southern Negev and yields higher intensity rainfall, thus being more similar to the radar observations.

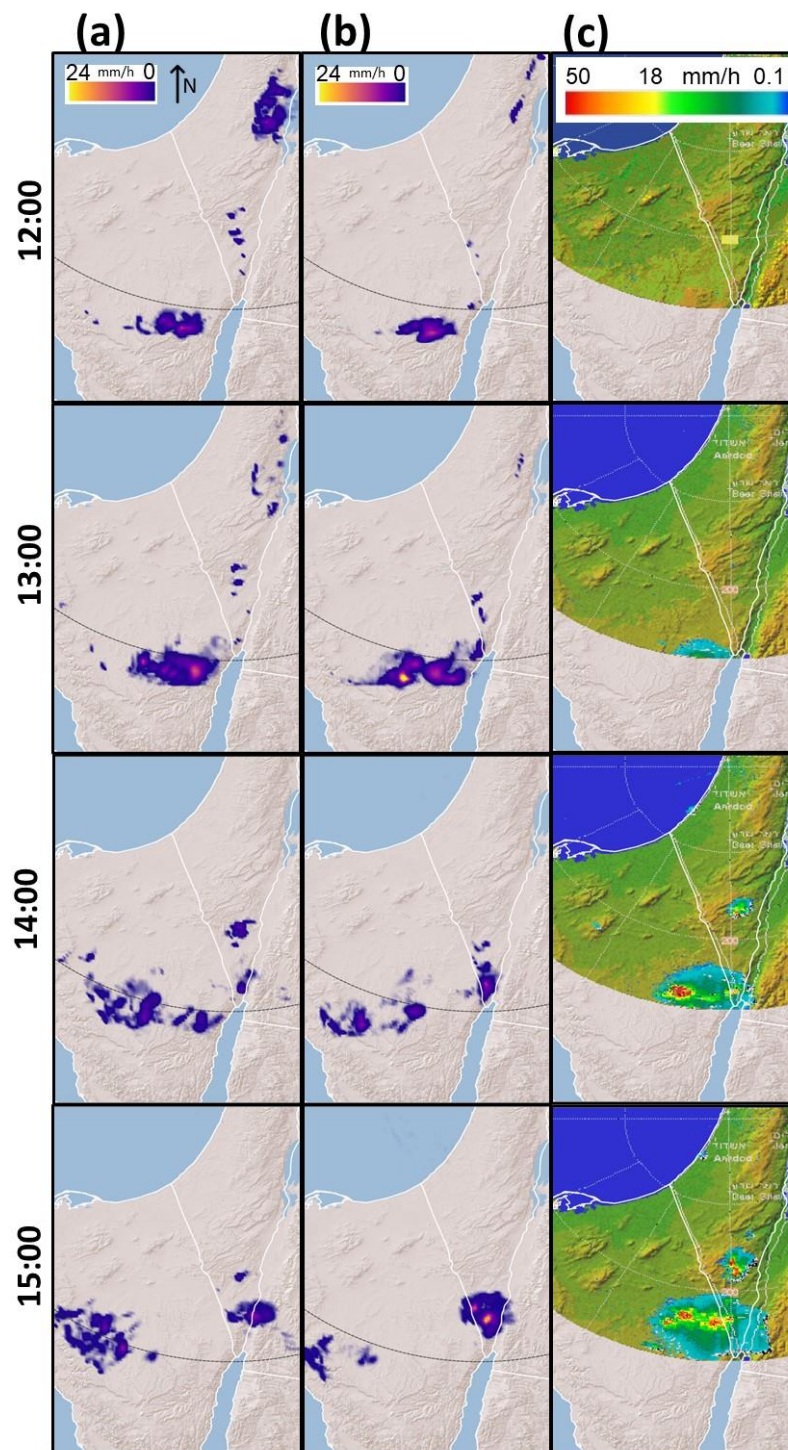


**Figure 6.** Results of WRF simulations on 15 September 2015, (a) with the Grell 3D ensemble convection scheme, (b) with the Kain–Fritsch convection scheme, and (c) the observed precipitation from the Israeli Meteorological Service radar.

#### Cloud Detection

We used MSG data to detect the timing and location of the first convective cell that later produced the floods of the 15 September 2015 event in the Negev. Figure 7 shows the earliest detection of the storm in its developing stages over the South Sinai Peninsula using three methods. The first convective cloud (indicated by a yellow circle in the images) can be seen in the RGB Day Natural Colors (top row) image at 9:00 UTC, whereas using our TFACLM method (bottom row), it was detected 45 min earlier (at 8:15 UTC), while the

MSG “official” cloud mask (Eumetsat CLM, middle row) detected this cloud at 8:45 UTC, 30 min later than the first detection by TFACLM.

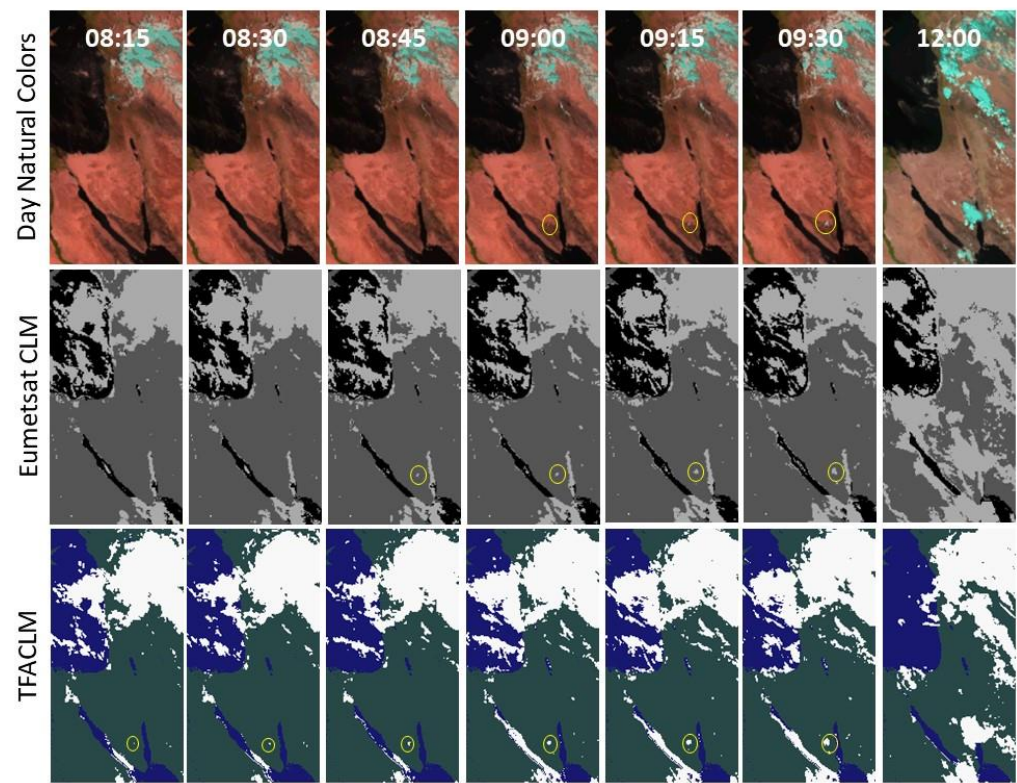


**Figure 7.** Time series of MSG satellite images over Israel and the Sinai Peninsula from 15 September 2015, with RGB Day Natural Colors in the upper row, Eumetsat cloud mask in the middle row, and TFACLM cloud mask in the lower row. The convective cloud (yellow circle) was first detected in the RGB image at 9:00 UTC, by Eumetsat CLM at 8:45 UTC, whereas TFACLM detected it earliest, at 8:15 UTC. Note the cloud cover differences between the Eumetsat CLM and TFACLM. A more detailed comparison of the two cloud masks is presented in Figure 8.

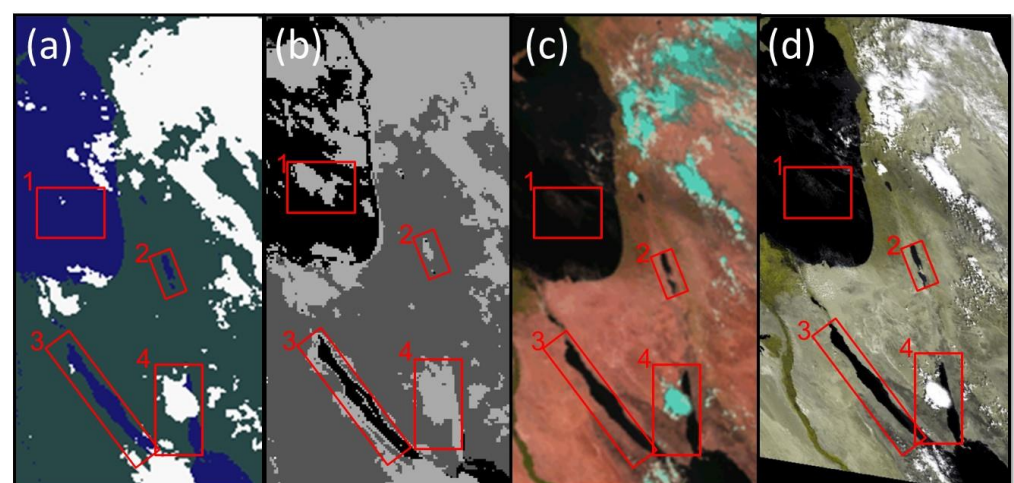


**Figure 8.** Comparison of (a) TFACLM and (b) EumetsatCLM products on 15 September 2015 at 11:15 UTC with (c) MSG RGB Day Natural Colors, and (d) MODIS-Aqua natural colors with 250 m resolution as a ground truth. The red boxes are plotted to assist in comparing the two cloud masks’ performance (for details, see text in the paragraph above).

Cloud mask algorithms can range from clear-conservative to cloud-conservative, meaning that if there is ambiguity in the algorithm logic, it classifies the pixel as either cloudy or cloud-free, respectively. Figure 8 demonstrates that the EUMETSAT CLM has a more clear-conservative tendency, e.g., in areas 3 and 4, EUMETSAT CLM overestimates cloud cover over the shorelines of the Gulf of Suez (box 3) and over the southern half of the Gulf of Eilat (box 4), whereas TFACLM marks most of these shorelines as clear-sky. The much higher resolution (250 m) MODIS image in Figure 8c,d confirms that the TFACLM performs better in those cases. Yet EUMETSAT CLM fails to flag the pixels of the evolving event as a cloud in its early stages (Figure 7—8:15 UTC). An opposite case is displayed in Figure 8a, where TFACLM does not flag the transparent clouds over the sea in area 1 as cloudy pixels, whereas the clear-conservative EUMETSAT CLM algorithm flags most of the pixels in this area as cloudy. Another example of the over-sensitivity of the EUMETSAT CLM algorithm over water can be seen in area 2 (the Dead Sea).

#### 4. Discussion and Conclusions

Accurately predicting convective storms is a complex task that includes the challenges of both convective initiation and convective evolution [38]. In the case of the Paran event analyzed in this paper, we showed that both had been successfully identified by the satellite data.

On 15 September 2015, an extreme flash flood occurred in southern Negev, Israel. The intensities of such flash floods occur only once in 50 years [14]. The forecast model used by the Israel Water Authority at that time missed this event. In this study, we analyzed this event and showed that the combined use of radar, satellite, and radiosonde data can provide important information regarding the potential for a flooding event. We also reran the forecast model and showed that changing the convective parameterization scheme can potentially improve the model to predict floods.

As is usually the case in RST systems in arid regions, the duration of the entire event was very short. The IMS radar detected the first occurrence of clouds in the Sinai Peninsula that day at 12:50 UTC (Figure 4). The event occurred nearly 250 km from the radar, near the end of its range, where the radar can detect only mature clouds with tops higher than 5 km and with large raindrops [39]. However, optical satellite observations can see clouds at much earlier stages and with much smaller droplets at the cloud top. Using RGB images of MSG SEVIRI visible channels, the clouds were first detected visually at 9:00 UTC (Figure 7). The MSG Cloud Mask (CLM) algorithms are sensitive to partly cloudy pixels. The official Eumetsat CLM detected the first occurrence of the cloud at 8:45 UTC, whereas our TFACLM detected the cloud 30 min earlier at 8:15 UTC (Figure 7). Not all clouds will develop a convective storm, thus detecting the first occurrence of a cloud is not sufficient. Monitoring the cloud development a few time steps ahead and looking for other convection indicators can support the decision whether to flag convective initiation. In our case, the indicators of subfreezing cloud top and significant cooling rates were detected already at 9:30 UTC. The yellow color, which is the distinct color of severe convection in the Convective Storms RGB, was seen at 11:15, whereas the first detection of precipitation by the radar was only seen at 12:50. The Paran watershed is primarily uninhabited, with a few roads crossing its area. The hydrometric station 57190 is near Highway 90, the major road traversed by most traffic to and from the port city of Eilat. The flood's first wave reached station 57190 at 18:40 UTC, with a flow rate peak at 19:30 UTC (Figure 2), more than 10 h after the first detection, and 9 h after the indicators of subfreezing cloud top and significant cooling rates were detected. Nowcasting the event using this information could provide an early warning.

Analyzing the vertical profiles of the cloud top temperature (T)–particle effective radius ( $r_e$ ) relationship of this event revealed the occurrence of a severe convective storm with strong updrafts and small ice particles at the cloud top (Figure 5). This distinction is strongly supported by the Convective Storms RGB images (Figure 5).

Atmospheric instability is a critical factor in the development of severe weather. NWP models provide atmospheric instability indices that show the potential for convection

development in the atmosphere. In the case of Paran's event, the model failed to predict instability. On the other hand, using a satellite cloud detecting technique along with ongoing analysis of the  $T-r_e$  curves and tracking the Convective Storms RGB and Day Microphysical RGB images of the evolving event showed that a convective storm is developing over the Sinai Peninsula.

Detecting clouds at an early stage by satellites can be used to initialize convective cells in NWP models and gain better predictions of the developing storm [40].

Data assimilation is the process through which observations are injected into the model's forecast cycles to increase forecast skill [41]; however, data assimilation has some limitations. It is restricted by the model resolution; therefore, assimilated data need to be upscaled to the model resolution. This means that observed weather features too small for the model to resolve correctly are left out of the analysis [42]. Moreover, extreme or rapidly changing situations, such as Paran's event, may not be handled well in the analysis [43]. Since these are precisely the situations in remote, unpopulated, arid areas, in which the model's initial conditions are likely to be poor and the forecast unreliable, the forecaster's challenge is to recognize potentially extreme or rapidly evolving weather events and place more emphasis on satellite analysis and other observations in developing a forecast, rather than leaning on NWP models alone. Combining the TFACLM with Convective Storms RGB and Day Microphysical RGB could provide the trigger to rerun the NWP model with an adequate scheme. In our case, initial clouds were observed at 8:15 UTC, and the cloud evolution revealed a convective storm already at 13:00 UTC. These are solid signs of a convective storm, which could be used for providing an alert based on satellite observations and for rerunning the NWP model with an alternative convective scheme, as was performed in this study. For this case, the WRF with the Kain–Fritsch scheme performed better than the Grell 3D. Throughout the event, it produced more intense rainfall and better simulated the location of the convective cells, thus being more consistent with the radar observations. Other studies of the sensitivity of WRF precipitation to the choice of the convective parameterization scheme [44] have also shown that mass-flux schemes, in general, and the Kain–Fritsch scheme, in particular, perform better than other convective schemes in semi-arid regions.

**Author Contributions:** Conceived and designed the experiments: S.S., I.M.L., and S.B. Dataset preparation: S.S. and A.G. Data validation: S.S. and A.G. Code and software preparation: S.S. writing—original draft preparation: S.S. writing—review and editing: S.S., A.G., S.B., and I.M.L. visualization: S.S. and A.G. supervision, project administration and funding acquisition: S.B. and I.M.L. All authors have read and agreed to the published version of the manuscript.

**Funding:** This research was funded by Israel Water Authority, grant number 4500963047, and Israel Meteorological Services.

**Data Availability Statement:** Data was obtained from Eumetsat (<https://www.eumetsat.int/eumetsat-data-centre>), NASA (<https://earthengine.google.com/>), IMS (<https://ims.gov.il/en>).

**Acknowledgments:** Israel Water Authority for the hydrological data, Israel Meteorological Services for the radar imagery, Eumetsat for the MSG data and the CLM product, NASA for the MODIS data, and University of Wyoming for the Radiosonde data.

**Conflicts of Interest:** The authors declare no conflict of interest. The funders had no role in the design of the study; in the collection, analyses, or interpretation of data; in the writing of the manuscript; or in the decision to publish the results.

## References

1. Alpert, P.; Krichak, S.O.; Shafir, H.; Haim, D.; Osetinsky, I. Climatic Trends to Extremes Employing Regional Modeling and Statistical Interpretation over the E. Mediterranean. *Glob. Planet. Chang.* **2008**, *63*, 163–170. [[CrossRef](#)]
2. Lin, X. Flash Floods in Arid and Semi-Arid Zones. In *IHP-V Technical Documents in Hydrology*; No. 23; UNESCO: Paris, France, 1999.
3. Marchi, L.; Borga, M.; Preciso, E.; Gaume, E. Characterisation of Selected Extreme Flash Floods in Europe and Implications for Flood Risk Management. *J. Hydrol.* **2010**, *394*, 118–133. [[CrossRef](#)]

4. Rinat, Y.; Marra, F.; Armon, M.; Metzger, A.; Levi, Y.; Khain, P.; Vadislavsky, E.; Rosensaft, M.; Morin, E. Hydrometeorological Analysis and Forecasting of a 3d Flash-Flood-Triggering Desert Rainstorm. *Nat. Hazards Earth Syst. Sci.* **2021**, *21*, 917–939. [[CrossRef](#)]
5. Ashbel, D. Great Floods in Sinai Peninsula, Palestine, Syria and the Syrian Desert, and the Influence of the Red Sea on Their Formation. *Q. J. R. Meteorol. Soc.* **1938**, *64*, 635–639. [[CrossRef](#)]
6. Kahana, R.; Ziv, B.; Enzel, Y.; Dayan, U. Synoptic Climatology of Major Floods in the Negev Desert, Israel. *Int. J. Climatol.* **2002**, *22*, 867–882. [[CrossRef](#)]
7. Tsvieli, Y.; Zangvil, A. Synoptic Climatological Analysis of Red Sea Trough and Non-Red Sea Trough Rain Situations over Israel. *Adv. Geosci.* **2007**, *12*, 137–143. [[CrossRef](#)]
8. Dayan, U.; Lensky, I.M.; Ziv, B.; Khain, P. Atmospheric Conditions Leading to an Exceptional Fatal Flash Flood in the Negev Desert, Israel. *Nat. Hazards Earth Syst. Sci.* **2021**, *21*, 1583–1597. [[CrossRef](#)]
9. Sharon, D.; Kutiel, H. The Distribution of Rainfall Intensity in Israel, Its Regional and Seasonal Variations and Its Climatological Evaluation. *J. Climatol.* **1986**, *6*, 277–291. [[CrossRef](#)]
10. Dayan, U.; Ziv, B.; Margalit, A.; Morin, E.; Sharon, D. A Severe Autumn Storm over the Middle-East: Synoptic and Mesoscale Convection Analysis. *Theor. Appl. Clim.* **2001**, *69*, 103–122. [[CrossRef](#)]
11. Tsvieli, Y.; Zangvil, A. Synoptic Climatological Analysis of ‘Wet’ and ‘Dry’ Red Sea Troughs over Israel. *Int. J. Climatol.* **2005**, *25*, 1997–2015. [[CrossRef](#)]
12. Saaroni, H.; Harpaz, T.; Alpert, P.; Ziv, B. Automatic Identification and Classification of the Northern Part of the Red Sea Trough and Its Application for Climatological Analysis. *Int. J. Climatol.* **2020**, *40*, 3607–3622. [[CrossRef](#)]
13. Ziv, B.; Saaroni, H.; Etkin, A.; Harpaz, T.; Shendrik, L. Formation of Cyclones over the East Mediterranean within Red-Sea Troughs. *Int. J. Climatol.* **2022**, *42*, 577–596. [[CrossRef](#)]
14. Givati, A.; Siegel, E.; Galili, U.; Paz, D. *Summary of the Exceptional Flood Events that Were Measured in the Fall of 2015*; Israel Water Authority: Jerusalem, Israel, 2015. (In Hebrew)
15. Schmetz, J.; Pili, P.; Tjemkes, S.; Just, D.; Kerkmann, J.; Rota, S.; Ratier, A. An Introduction to Meteosat Second Generation (MSG). *Bull. Am. Meteorol. Soc.* **2002**, *83*, 977–992. [[CrossRef](#)]
16. Vermote, E.; Roger, J.C.; Ray, J. *MODIS Surface Reflectance User’s Guide*; MODIS Land Surface Reflectance Science Computing Facility; USGS: Reston, VA, USA, 2015.
17. Mereu, L.; Marzano, F.S.; Montopoli, M.; Bonadonna, C. Retrieval of Tephra Size Spectra and Mass Flow Rate From C-Band Radar During the 2010 Eyjafjallajökull Eruption, Iceland. *IEEE Trans. Geosci. Remote Sens.* **2015**, *53*, 5644–5660. [[CrossRef](#)]
18. Shentsis, I.; Laronne, J.B.; Alpert, P. Red Sea Trough Flood Events in the Negev, Israel (1964–2007). *Hydrol. Sci. J.* **2012**, *57*, 42–51. [[CrossRef](#)]
19. Moncrieff, M.W.; Miller, M.J. The Dynamics and Simulation of Tropical Cumulonimbus and Squall Lines. *Q. J. R. Meteorol. Soc.* **1976**, *102*, 373–394. [[CrossRef](#)]
20. Givati, A.; Lynn, B.; Liu, Y.; Rimmer, A. Using the WRF Model in an Operational Streamflow Forecast System for the Jordan River. *J. Appl. Meteorol. Climatol.* **2012**, *51*, 285–299. [[CrossRef](#)]
21. Grell, G.A.; Dévényi, D. A Generalized Approach to Parameterizing Convection Combining Ensemble and Data Assimilation Techniques. *Geophys. Res. Lett.* **2002**, *29*, 38-1–38-4. [[CrossRef](#)]
22. Kain, J.S. The Kain–Fritsch Convective Parameterization: An Update. *J. Appl. Meteorol.* **2004**, *43*, 170–181. [[CrossRef](#)]
23. Rossow, W.B. Measuring Cloud Properties from Space: A Review. *J. Clim.* **1989**, *2*, 201–213. [[CrossRef](#)]
24. Ackerman, S.A.; Frey, R.A. *MODIS Atmosphere L2 Cloud Mask Product 2015*; NASA: Greenbelt, MD, USA, 2015.
25. Derrien, M.; Le Gléau, H. MSG/SEVIRI Cloud Mask and Type from SAFNWC. *Int. J. Remote Sens.* **2005**, *26*, 4707–4732. [[CrossRef](#)]
26. Scharlemann, J.P.W.; Benz, D.; Hay, S.I.; Purse, B.V.; Tatem, A.J.; Wint, G.R.W.; Rogers, D.J. Global Data for Ecology and Epidemiology: A Novel Algorithm for Temporal Fourier Processing MODIS Data. *PLoS ONE* **2008**, *3*, e1408. [[CrossRef](#)]
27. Lensky, I.M.; Dayan, U. Detection of Fine-Scale Climatic Features from Satellites and Implications to Agricultural Planning. *Bull. Am. Meteorol. Soc.* **2011**, *92*, 1131–1136. [[CrossRef](#)]
28. Lensky, I.M.; Rosenfeld, D. Clouds–Aerosols–Precipitation Satellite Analysis Tool (CAPSAT). *Atmos. Chem. Phys.* **2008**, *8*, 6739–6753. [[CrossRef](#)]
29. Rosenfeld, D.; Woodley, W.L.; Lerner, A.; Kelman, G.; Lindsey, D.T. Satellite Detection of Severe Convective Storms by Their Retrieved Vertical Profiles of Cloud Particle Effective Radius and Thermodynamic Phase. *J. Geophys. Res.* **2008**, *113*. [[CrossRef](#)]
30. Rosenfeld, D.; Lensky, I.M. Satellite-Based Insights into Precipitation Formation Processes in Continental and Maritime Convective Clouds. *Bull. Am. Meteorol. Soc.* **1998**, *79*, 2457–2476. [[CrossRef](#)]
31. Hansen, J.E.; Travis, L.D. Light Scattering in Planetary Atmospheres. *Space Sci. Rev.* **1974**, *16*, 527–610. [[CrossRef](#)]
32. Lensky, I.M.; Rosenfeld, D. The Time-Space Exchangeability of Satellite Retrieved Relations between Cloud Top Temperature and Particle Effective Radius. *Atmos. Chem. Phys.* **2006**, *6*, 2887–2894. [[CrossRef](#)]
33. Huang, Y.; Meng, Z.; Li, J.; Li, W.; Bai, L.; Zhang, M.; Wang, X. Distribution and Variability of Satellite-Derived Signals of Isolated Convection Initiation Events over Central Eastern China. *J. Geophys. Res. Atmos.* **2017**, *122*, 11357–11373. [[CrossRef](#)]
34. Roberts, R.D.; Rutledge, S. Nowcasting Storm Initiation and Growth Using GOES-8 and WSR-88D Data. *Weather Forecast.* **2003**, *18*, 562–584. [[CrossRef](#)]
35. Mecikalski, J.R.; Bedka, K.M. Forecasting Convective Initiation by Monitoring the Evolution of Moving Cumulus in Daytime GOES Imagery. *Mon. Weather Rev.* **2006**, *134*, 49–78. [[CrossRef](#)]

36. Siewert, C.W.; Koenig, M.; Mecikalski, J.R. Application of Meteosat Second Generation Data towards Improving the Nowcasting of Convective Initiation. *Meteorol. Appl.* **2010**, *17*, 442–451. [[CrossRef](#)]
37. Zangvil, A.; Druian, P. Upper Air Trough Axis Orientation and the Spatial Distribution of Rainfall over Israel. *Int. J. Climatol.* **1990**, *10*, 57–62. [[CrossRef](#)]
38. Weygandt, S.S.; Benjamin, S.G.; Hu, M.; Alexander, C.R.; Smirnova, T.G.; James, E.P. Radar Reflectivity-Based Model Initialization Using Specified Latent Heating (Radar-LHI) within a Diabatic Digital Filter or Pre-Forecast Integration. *Weather Forecast.* **2022**, *37*, 1419–1434. [[CrossRef](#)]
39. Min, C.; Chen, S.; Gourley, J.J.; Chen, H.; Zhang, A.; Huang, Y.; Huang, C. Coverage of China New Generation Weather Radar Network. *Adv. Meteorol.* **2019**, *2019*, e5789358. [[CrossRef](#)]
40. Gregow, E.; Lindfors, A.V.; van der Veen, S.H.; Schoenach, D.; de Haan, S.; Lindskog, M. The Use of Satellite and Surface Observations for Initializing Clouds in the HARMONIE NWP Model. *Meteorol. Appl.* **2020**, *27*, e1965. [[CrossRef](#)]
41. Kwon, I.-H.; English, S.; Bell, W.; Potthast, R.; Collard, A.; Ruston, B. Assessment of Progress and Status of Data Assimilation in Numerical Weather Prediction. *Bull. Am. Meteorol. Soc.* **2018**, *99*, ES75–ES79. [[CrossRef](#)]
42. Mohandas, S. Weather and Climate Modeling. In *Social and Economic Impact of Earth Sciences*; Gahalaut, V.K., Rajeevan, M., Eds.; Springer Nature: Singapore, 2023; pp. 121–141; ISBN 978-981-19692-9-4.
43. Castorina, G.; Caccamo, M.T.; Insinga, V.; Magazù, S.; Munaò, G.; Ortega, C.; Semprebello, A.; Rizza, U. Impact of the Different Grid Resolutions of the WRF Model for the Forecasting of the Flood Event of 15 July 2020 in Palermo (Italy). *Atmosphere* **2022**, *13*, 1717. [[CrossRef](#)]
44. Musa, A.I.I.; Tsubo, M.; Ma, S.; Kurosaki, Y.; Ibaraki, Y.; Ali-Babiker, I.-E.A. Evaluation of WRF Cumulus Parameterization Schemes for the Hot Climate of Sudan Emphasizing Crop Growing Seasons. *Atmosphere* **2022**, *13*, 572. [[CrossRef](#)]

**Disclaimer/Publisher’s Note:** The statements, opinions and data contained in all publications are solely those of the individual author(s) and contributor(s) and not of MDPI and/or the editor(s). MDPI and/or the editor(s) disclaim responsibility for any injury to people or property resulting from any ideas, methods, instructions or products referred to in the content.